USE OF LOWTRAN DERIVED ATMOSPHERIC PARAMETERS IN SYNTHETIC IMAGE GENERATION MODELS

Carl Salvaggio, Joseph D. Sirianni and John R. Schott

Rochester Institute of Technology
Center for Imaging Science
Digital Imaging and Remote Sensing Laboratory
Chester F. Carlson Building
P.O. Box 9887
Rochester, New York 14623-0887

ABSTRACT

The Digital Imaging and Remote Sensing laboratory's Image Generation model, DIRSIG, combines computer aided design (CAD), ray tracing techniques, radiometric principles, and thermodynamic models to create synthetic imagery. The model emphasizes rigorous radiometric solutions that account for spectral reflectance effects, angular emissivities, atmospheric transmission and upwelled and downwelled sky radiance. This paper describes enhancements to the radiometric portion of the code that permits inclusion of variations with azimuth of downwelling sky radiance, solution of the radiometric propagation models using specific radiosonde data including adjustments for the time of day, and the incorporation of background effects from objects adjacent to the target. Simulated scenes are presented that show how these enhancements produce imagery that more closely match observed phenomena. In particular, the importance of properly modeled sky radiance is shown both for low altitude oblique imagery where the sky is directly observed and for near nadir imagery where reflected sky radiance is important.

INTRODUCTION

The use of synthetic scene generation models provides an excellent tool for many research aspects involved with the collection of remotely sensed imagery. New sensor designs can be specified and tested without having to go through the expense of actually building the system; analysts can experiment with the many different environmental parameters which affect the radiance field propagated through the atmosphere to see if the phenomena they assume is causing an effect in a scene is indeed the source; realistic scenarios in flight simulation can better prepare pilots for the conditions they might encounter; academics can better instruct their students on the physical phenomena that impact image collection. All these, and the many other applications, demonstrate a need for accurate synthetic scene generation capabilities.

DIRSIG provides a radiometrically rigorous treatment of the physical phenomena affecting a remote sensing imaging system. It provides imagery representing the primary radiance field reaching the front end of an imaging system. Using techniques from the discipline of computer graphics, ray tracing is used to produce the geometric frame on which radiance values are laid. A computer aided design package such as AutoCAD (AutoCAD, 1989) is used to construct objects and place them together to form a scene. This scene which is formed of objects made up of 3- and 4-sided facets, is input to a ray tracing model which is capable of determining the many geometric and situation specific parameters affecting the formation of the upwelling radiance field. Using some simple ray tracing algorithms, as those described by Haines, 1987, and an attributed data structure attached to each facet,

0-8194-1174-4/93/$6.00

information such as object intersection points, target material type, material object parameters (emissivity, reflectivity, thermal conductivity, thermal "thickness"), background objects in the specular bounce direction, and propagation path length can be determined. The procedures and details of this implementation are described by Schott *et al.*, 1992.

The database of information formed by ray tracing a single pixel is then used to accurately predict the radiance emanating from that point in the scene. For the self-emitted portion of the radiance field, the thermal properties for the material type encountered along with a detailed weather history describing the target's environment for up to 24-hours preceding the simulated acquisition serve as input to a differential thermodynamic model, THERM (DCS Corporation, 1991). This model predicts target temperatures which track well with actual phenomena (Rankin et al., 1992). The reflected portion of the spectrum relies on prediction of atmospheric radiance data using the MODTRAN atmospheric transmission and path radiance code (Berk *et al.*, 1989). This moderate spectral resolution model based on the LOWTRAN 7 code (Kneizys et al., 1989) allows prediction of atmospheric transmission along the sensor-target and target-sun paths, self-emitted and solar scattered upwelled path radiance, and with some modification self-emitted and solar downwelled sky radiance.

This paper will address recent progress made in the development of the radiometric model used in the DIRSIG code. Specifically, issues concerning the following will be addressed: inclusion of variations with azimuth of downwelling sky radiance, solution of the radiometric propagation models using specific radiosonde data including adjustments for the time of day, and the incorporation of background effects from objects adjacent to the target.

TECHNICAL APPROACH

The radiance field reaching the sensor defined by the DIRSIG model is representative of one of four imaging scenarios. The ray cast from the sensor to the scene will result in one of the following (as illustrated in Figure 1): the ray will encounter a diffuse target, the ray

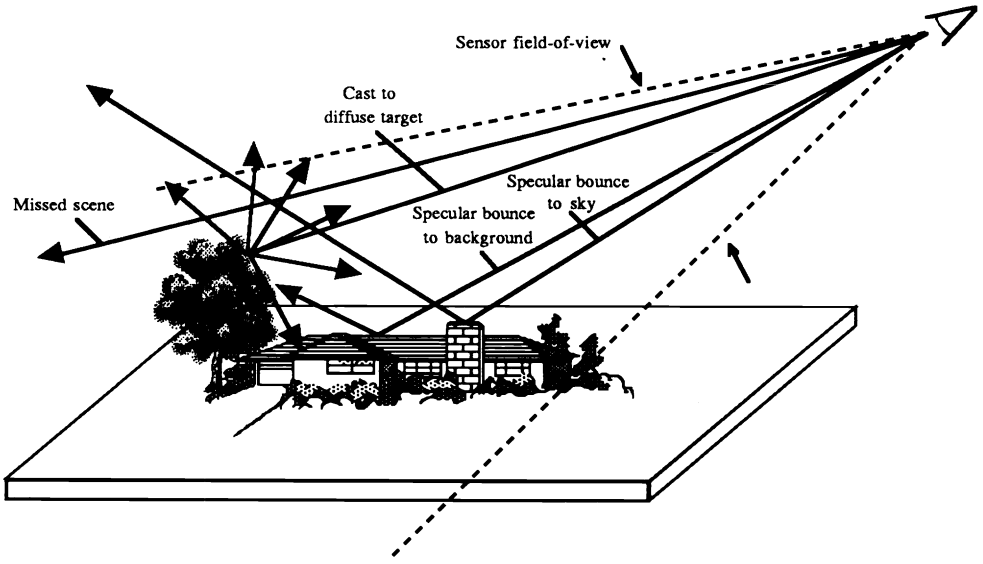

Figure 1 Illustration of the four possible ray/scene interactions that are accounted for in the DIRSIG model.

will encounter a specular target and bounce to the sky, the ray will encounter a specular object and bounce to an in-scene background, or the ray will miss all scene elements and hit the sky.

The spectral radiance reaching a sensor from a target with specular reflectance characteristics is described by

$$
\begin{aligned}
L(\theta,\phi,\lambda) = \Bigg\{ & \varepsilon_T(\theta,\lambda)L_T(\lambda) + \\
& \Bigg[I_T \frac{E_S(\lambda)}{\pi} \tau_1(\lambda)\cos(\theta_S) + \\
& F[L_{DE}(\theta_{SK},\phi_{SK},\lambda) + L_{DS}(\theta_{SK},\phi_{SK},\lambda)] + \\
& (1-F)\Big\{\varepsilon_B(\theta_{BT},\lambda)L_{TB}(\lambda) + \\
& I_B \frac{E_S(\lambda)}{\pi} \tau_1(\lambda)\cos(\theta_B)[1-\varepsilon_B(\theta_{BT},\lambda)]\Big\}\Bigg] \\
& [1-\varepsilon_T(\theta,\lambda)]\Bigg\} \\
& \tau_2(\theta_E,p,\lambda) + L_{uE}(\theta_E,p,\lambda) + L_{uS}(\theta_E,p,\lambda)
\end{aligned}
\tag{1}
$$

where the shape factor F is set to unity when the specular ray bounces to the sky or to zero for a bounce to a background object. The spectral reflectance for a target exhibiting diffuse reflectance characteristics is given by

$$
\begin{aligned}
L(\theta,\phi,\lambda) = \Bigg\{ & \varepsilon_T(0,\lambda)L_T(\lambda) + \\
& \Bigg[I_T \frac{E_S(\lambda)}{\pi} \tau_1(\lambda)\cos(\theta_S) + \\
& F[L_{DE}(\lambda) + L_{DS}(\lambda)] + \\
& (1-F)\Big\{\varepsilon_B(\theta_{BT},\lambda)L_{TB}(\lambda) + \\
& I_B \frac{E_S(\lambda)}{\pi} \tau_1(\lambda)\cos(\theta_B)[1-\varepsilon_B(\theta_{BT},\lambda)]\Big\}\Bigg] \\
& [1-\varepsilon_T(0,\lambda)]\Bigg\} \\
& \tau_2(\theta_E,p,\lambda) + L_{uE}(\theta_E,p,\lambda) + L_{uS}(\theta_E,p,\lambda)
\end{aligned}
\tag{2}
$$

where the background emitted radiance, $L_{TB}(\lambda)$, is the radiance due to a blackbody at a temperature, TB, equal to the average temperature of all possible background objects to which the target is exposed, while the emissivity, $\varepsilon_B(\theta_{BT},\lambda)$, is the angular spectral emissivity of the most common background to which the target is exposed. This method is

carried out as an approximation of the numerical integration of the radiance emitted by all background objects which are visible from the target.

The final integrated radiance field is computed as the integral of the above spectral radiance values,

$$L(\theta,\phi) = \int_{\lambda} L(\theta,\phi,\lambda)\beta(\lambda)d\lambda \tag{3}$$

The variables used in Equations 1 through 3 are defined as follows (the subscript, λ, indicate wavelength specific values):

$L(\theta,\phi,\lambda)$	spectral radiance reaching the front end of the sensor
$E_S(\lambda)$	the exoatmospheric solar spectral irradiance
$L_T(\lambda)$	the self-emitted spectral radiance from a blackbody at temperature T (target)
$L_{TB}(\lambda)$	the self-emitted spectral radiance from a blackbody at temperature T (background)
$L_{DE}(\lambda)$	the downwelled spectral radiance due to self-emission of the atmosphere integrated over the skydome
$L_{DS}(\lambda)$	the downwelled spectral radiance due to scattering integrated over the skydome
$L_{DE}(\theta_{SK},\phi_{SK},\lambda)$	the directional downwelled spectral radiance due to self-emission of the atmosphere
$L_{DS}(\theta_{SK},\phi_{SK},\lambda)$	the directional downwelled spectral radiance due to scattering
$L_{uE}(\theta_E,p,\lambda)$	the upwelled spectral radiance due to self-emission of the atmosphere along the target-sensor path
$L_{uS}(\theta_E,p,\lambda)$	the upwelled spectral radiance due to scattering along the target-sensor path
$\tau_1(\lambda)$	the atmospheric spectral transmission along the source-target path
$\tau_2(\theta_E,p,\lambda)$	the atmospheric spectral transmission along the target -sensor path
$\varepsilon_T(\theta,\lambda)$	angular spectral emissivity for the target
$\varepsilon_B(\theta_{BT},\lambda)$	angular spectral emissivity for the background
I_T	a flag indicating whether the target is sunlit (1) or shadowed by another object (0)
I_B	a flag indicating whether the background is sunlit (1) or shadowed by another object (0)
θ	the angle between the normal to the surface and the sensor-target path
θ_S	the angle between the normal to the surface and the sun-target path
θ_B	the angle between the normal to the background and the sun-background path
θ_E	the angle between normal to the earth at the target and the sensor-target path
θ_{SK}	the angle between the normal to the earth and the specularly reflected ray from the sensor to target cast

θ_{BT}	the angle between the normal to the background and the target hit point
ϕ	the azimuth angle between the projection of the sensor-target path on the ground and the scene's reference direction
ϕ_{SK}	the azimuth angle between the projection of the ray cast to the sky on the ground and the scene's reference direction
F	shape factor, the fraction of exposed skydome
p	the range between the target and the sensor
$\beta(\lambda)$	the spectral response of the sensor

The angles utilized in Equations 1 through 3 are illustrated in Figure 2.

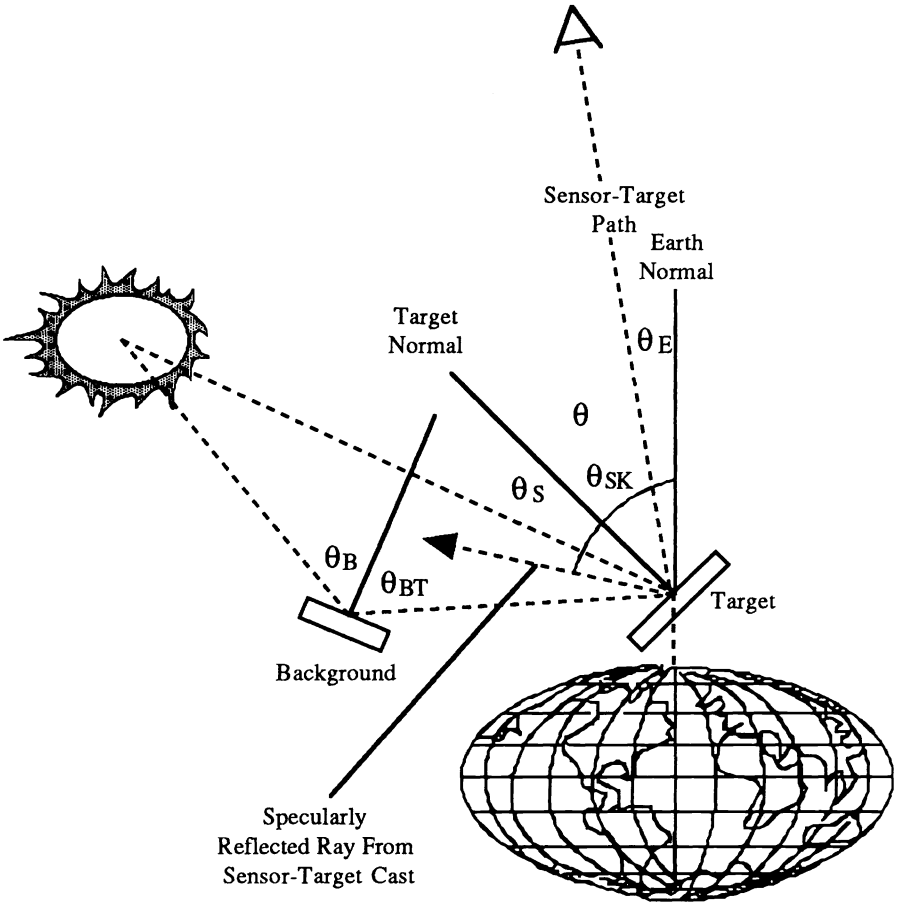

Figure 2 Illustration of the radiometric interation angles used in computing the radiance field reaching the sensor.

Directional downwelled radiance

To this point in the development of the DIRSIG model, the sky has been assumed to be isotropic with respect to azimuth. This implied that the downwelling sky radiance from a position in the west sky was identical to the radiance coming from the south sky at the same elevation. This assumption had arisen from the historical development of the code.

Originally a model capable only of working in the thermal infrared portion of the spectrum, the need for variations with azimuthal sky radiance was unnecessary. In this portion of the spectrum, the downwelled sky radiance is heavily dominated by self-emission and therefore was largely independent of solar position. Varying only with elevation (zenith) angle, downwelled radiance was assumed constant as one swept around the hemisphere. In portions of the spectrum where solar contributions to the downwelled radiance field are significant, the sky radiance field varies dramatically with azimuth as well as zenith. Figures 3 and 4 illustrates the variation in the radiance field with sky position in the self-emitted and reflective portions of the spectrum. In viewing these plots one will notice the brightening of the sky near the horizon, due to heavy scattering in the reflective portions of the spectra and large path lengths in the self-emitted case. These simulations match the actual physical phenomena which occur.

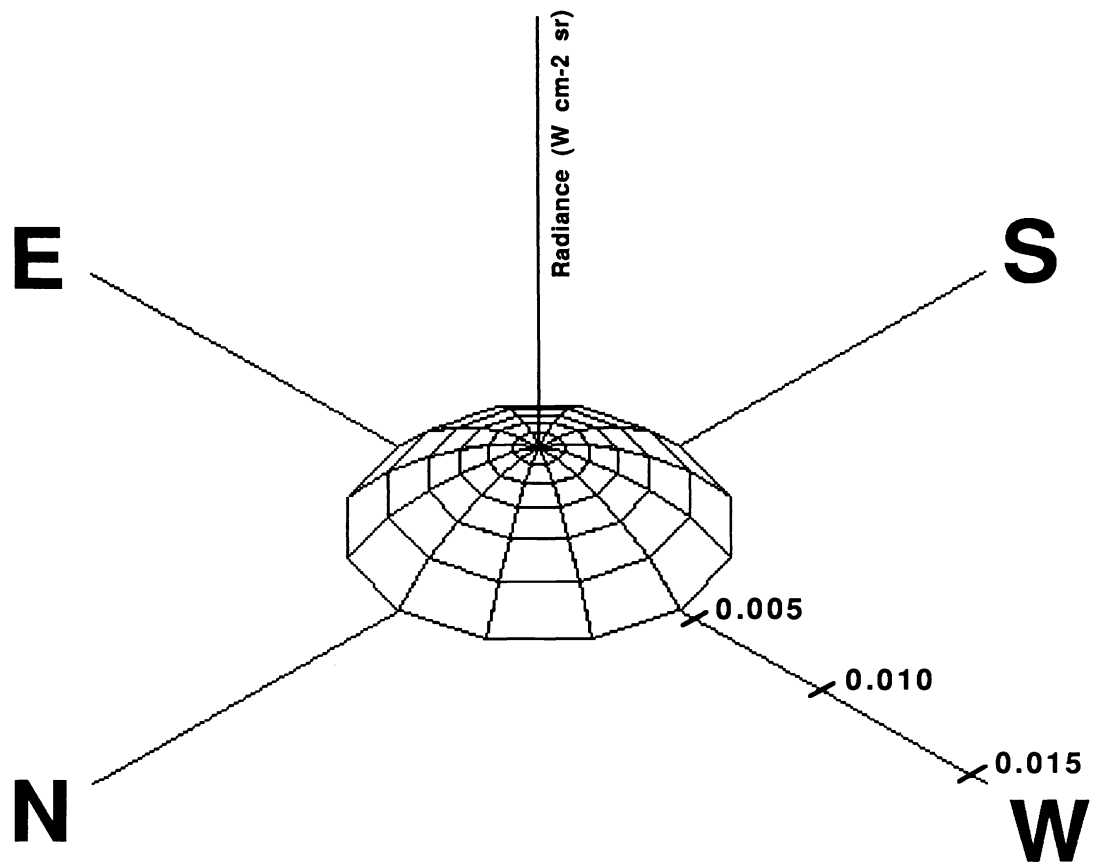

Figure 3 Spherical plot illustrating the downwelled sky radiance field in the 8 to 14 micron bandpass (longwave infrared portion of the spectrum, 750 to 1250 cm-1). Simulated radiance produced for the following conditions: 39°46'24"N latitude, 84°06'32"W longitude, day number 172, 9:00AM local time (14:00 GMT).

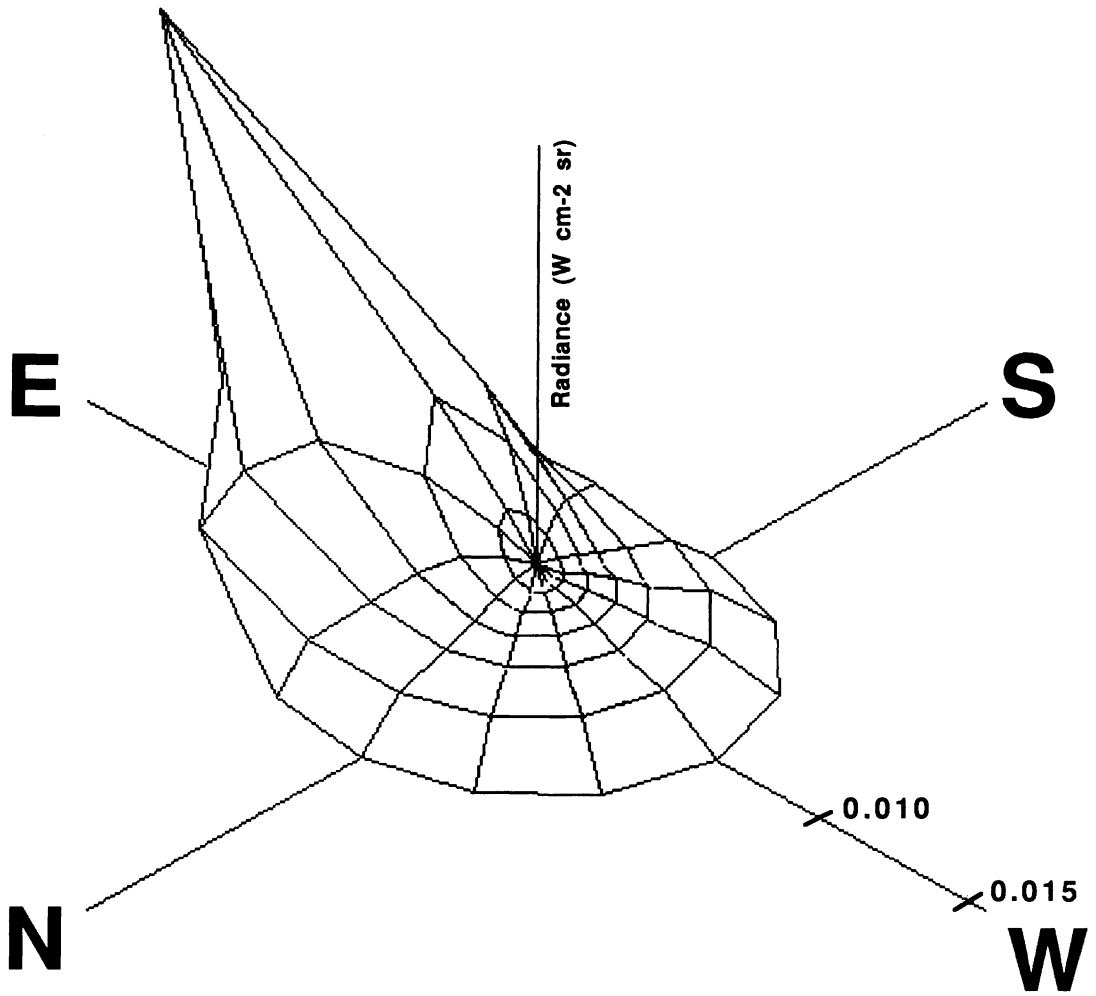

Figure 4 Spherical plot illustrating the downwelled sky radiance field in the 0.4 to 0.7 micron bandpass (visible portion of the spectrum, 14200 to 25000 cm-1). Simulated radiance produced for the following conditions: 39°46'24"N latitude, 84°06'32"W longitude, day number 172, 9:00AM local time (14:00 GMT).

In order to represent the hemispheric downwelled radiance field onto a scene, a database is formed using a modified version of the MODTRAN atmospheric propagation model. Depending on the nature of the target material encountered, the downwelling sky radiance is treated in a unique manner. For a specular target, directional downwelled radiance is determined for the particular portion of the sky which is in the reflected direction. For a diffuse target, an integrated hemispheric downwelled radiance value is computed. For either case, a database of sky radiance values is accessed which consists of spectral radiance as a function of azimuth and zenith angle, $L(\theta,\phi,\lambda)$. The database is defined on 15° increments in zenith from 0° (straight above) to 90° (horizon) and on 30° increments

from 0° (north-facing) to 360°. Figure 5 illustrates the layout of the downwelled radiance database.

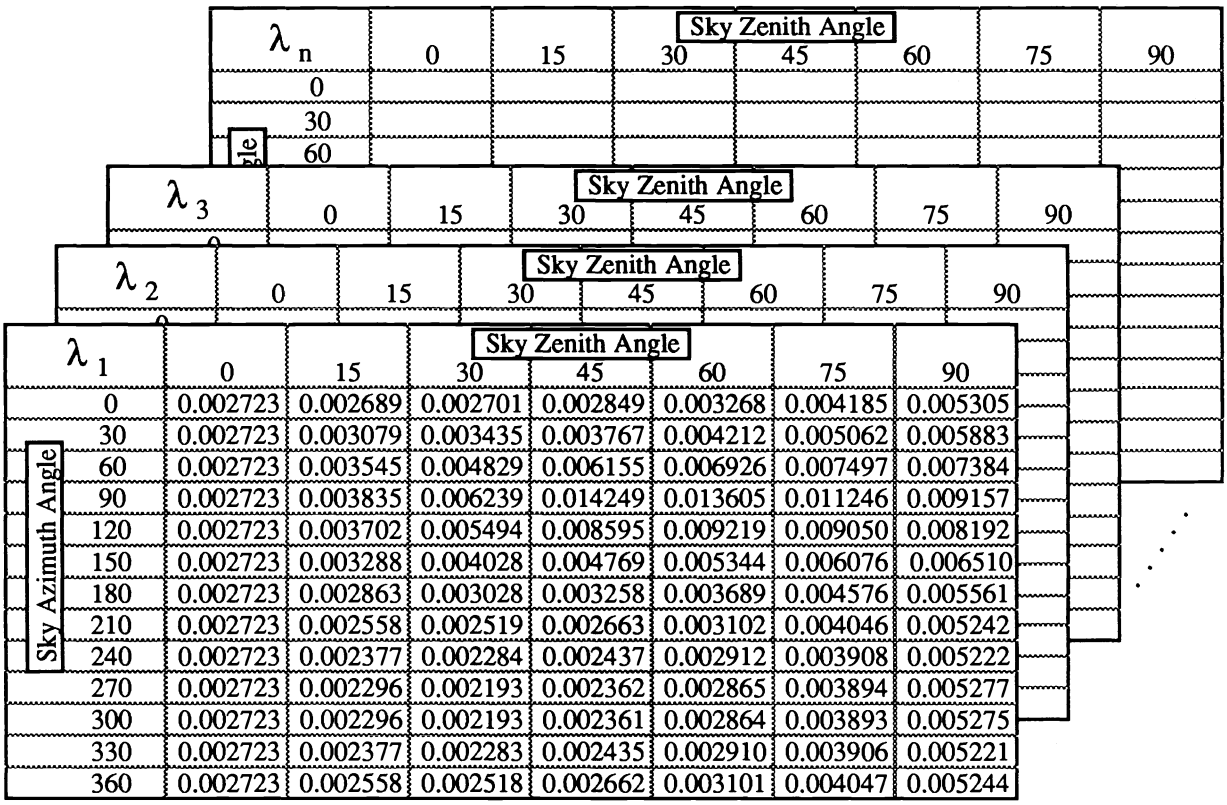

λ_1 Sky Azimuth Angle	Sky Zenith Angle 0	15	30	45	60	75	90
0	0.002723	0.002689	0.002701	0.002849	0.003268	0.004185	0.005305
30	0.002723	0.003079	0.003435	0.003767	0.004212	0.005062	0.005883
60	0.002723	0.003545	0.004829	0.006155	0.006926	0.007497	0.007384
90	0.002723	0.003835	0.006239	0.014249	0.013605	0.011246	0.009157
120	0.002723	0.003702	0.005494	0.008595	0.009219	0.009050	0.008192
150	0.002723	0.003288	0.004028	0.004769	0.005344	0.006076	0.006510
180	0.002723	0.002863	0.003028	0.003258	0.003689	0.004576	0.005561
210	0.002723	0.002558	0.002519	0.002663	0.003102	0.004046	0.005242
240	0.002723	0.002377	0.002284	0.002437	0.002912	0.003908	0.005222
270	0.002723	0.002296	0.002193	0.002362	0.002865	0.003894	0.005277
300	0.002723	0.002296	0.002193	0.002361	0.002864	0.003893	0.005275
330	0.002723	0.002377	0.002283	0.002435	0.002910	0.003906	0.005221
360	0.002723	0.002558	0.002518	0.002662	0.003101	0.004047	0.005244

Figure 5 Downwelled sky radiance database formed from repeated runs of the MODTRAN atmospheric transmission and path radiance code. The model is run in the vertical or slant path to space mode.

For specular targets, a simple bilinear interpolation method is used to determine the downwelled sky radiance, L_D, at the particular azimuth (ϕ) and zenith (θ) angle. The interpolation is depicted in Figure 6 and described in Equations 4 through 6 as

$$L_D(\theta,\phi,\lambda) = \frac{(\phi-\phi_2)(L_D(\theta,\phi_1,\lambda)-L_D(\theta,\phi_2,\lambda))}{\phi_1-\phi_2} + L_D(\theta,\phi_2,\lambda) \tag{4}$$

where

$$L_D(\theta,\phi_1,\lambda) = \frac{(\theta-\theta_1)(L_D(\theta_2,\phi_1,\lambda)-L_D(\theta_1,\phi_1,\lambda))}{\theta_2-\theta_1} + L_D(\theta_1,\phi_1,\lambda) \tag{5}$$

and

$$L_D(\theta,\phi_2,\lambda) = \frac{(\theta-\theta_1)(L_D(\theta_2,\phi_2,\lambda)-L_D(\theta_1,\phi_2,\lambda))}{\theta_2-\theta_1} + L_D(\theta_1,\phi_2,\lambda) \quad (6)$$

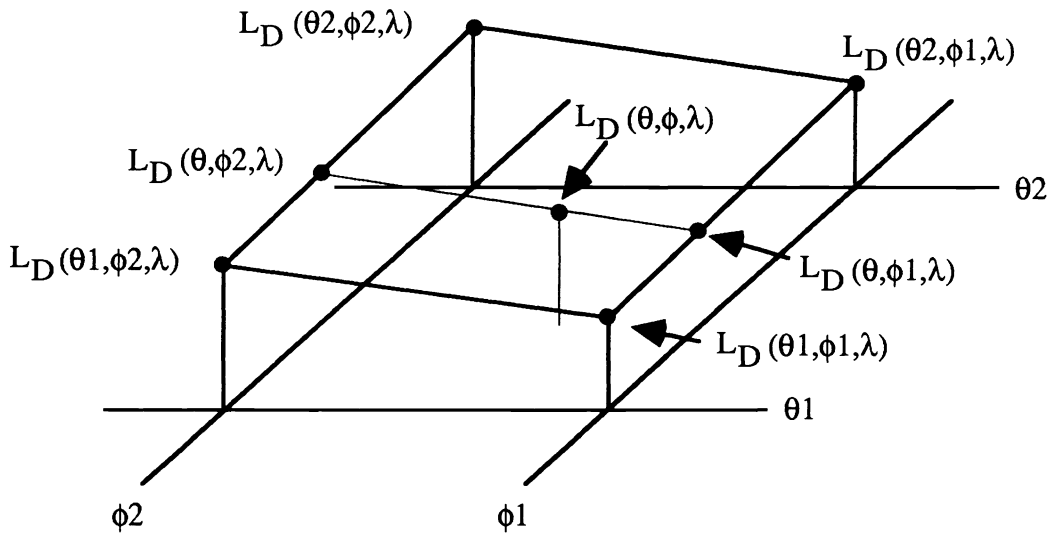

Figure 6 Illustration of the bilinear interpolation method for determining the downwelled sky radiance at a particular azimuth (ϕ) and zenith (θ) angle.

For a diffuse target, the directional downwelled radiance database described above is integrated over the hemisphere and spectral values are defined as

$$L_D(\lambda) = \int_{\phi=0}^{2\pi}\int_{\theta=0}^{\pi/2} L_D(\theta,\phi,\lambda)\cos(\theta)\sin(\theta)d\theta d\phi \quad (7)$$

The downwelled radiance values described in Equations 4 through 7 are based on repeated runs of the modified MODTRAN atmospheric transmission and path radiance code. Spectral values for the self-emitted and scattered solar downwelled radiance are extracted from the combined radiance field reported by MODTRAN and used to form two independent databases for each of these contributors. The quantities described in Equations 7 and 8 then correspond to those values used in Equations 1 and 2 describing the radiance field reaching the sensor for specular and diffuse targets. For example, $L_{DS}(\theta_{SK},\phi_{SK},\lambda)$, is the directional downwelled radiance due to solar scattering computed using Equation 6.

Sky fraction computation

The amount of "sky light" or downwelled radiance which is impinging on a target is determined by several factors including scattering and self-emission due to the atmosphere as well as obstruction by background objects. To this point, DIRSIG has assumed that each pixel in the scene which exhibited diffuse reflectance characteristics had an unobstructed hemisphere above it. In fact, the portion of the downwelling radiance field

from the hemisphere above the target is modified by adjacent background objects. Every object within a scene which extends above the plane formed by the target, obscures a portion of the sky, therefore, reducing the amount of radiance falling onto the target. The fraction of the sky to which a target is exposed is referred to as the target's shape factor, F. Figure 7 illustrates the effect that has been described.

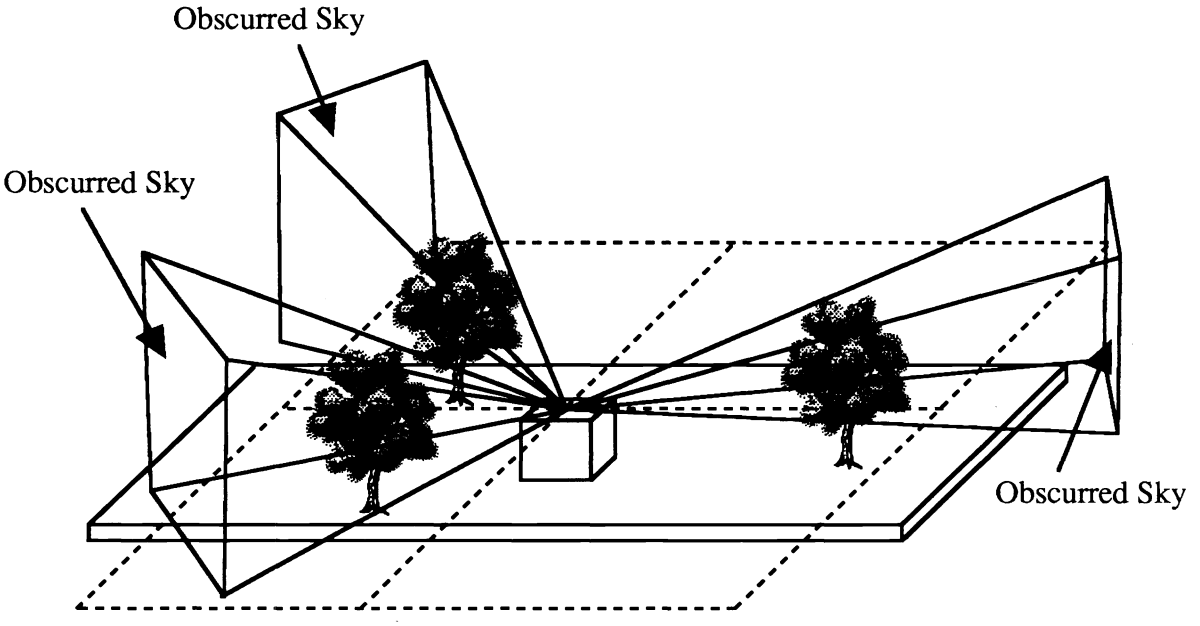

Figure 7 Background objects obscure a portion of the hemisphere above a scene element limiting the portion of the downwelled "sky radiance" field which can fall onto a target.

In order to determine the percent of non-obscured sky (shape factor, F), ray tracing techniques can be employed. A series of rays are cast out in a regular pattern over the entire hemisphere above the target. Once a primary hit point on the target has been defined, rays are cast out in a regular interval in azimuth and zenith and the number of rays which result in "hits" are recorded. The fraction of rays which hit an object weighted by the solid angle covered by each ray (1-F) is used to compute the portion of non-obscured sky or the shape factor (F). The shape factor is computed as

$$F = 1 - \frac{\sum_{\theta=0}^{\pi/2} \sum_{\phi=0}^{2\pi} h \sin(\theta) \Delta\theta \Delta\phi}{2\pi} \tag{8}$$

where θ and ϕ are the zenith and azimuth angle for each ray cast and h is a binary flag indicating whether or not the cast ray intersects a background object (1 if a hit occurs, 0 if the ray misses all background objects). The rays which are cast in the computation of the shape factor, have their origin at the point where the current scene ray hits the target of interest and a direction vector defined by (i,j,k) where

$$i = \cos\theta\cos\phi$$
$$j = \cos\theta\sin\phi \qquad (9)$$
$$k = \sin\theta$$

The resolution with which the azimuth and zenith angles are varied will affect the quality of the determined fraction. For this study, azimuth is stepped in 30° increments while zenith is changed in 15° increments.

In addition to determining the percentage of the sky which is obscured from the target, the procedure described above also serves to define the self-emitted and reflective portions of the background radiance contributions for background objects. While blocking the downwelled sky radiance from the target, these obstructions also serve as sources of energy which falls on the target. In the self-emitted portion of the spectrum, the kinetic temperature of these background objects create a source of incoming radiance for the target while in the reflective portion of the spectrum, they serve to reflect solar energy onto the target. During the procedure to determine the shape factor, each time a background object is encountered, it's material type and temperature are noted. When completed, the average temperature of all encountered background objects is computed and used for the term TB in Equation 2. The emissivity term, ε_B, in Equation 2 is defined as the most commonly occurring background during the search. For example, if 5 rays hit trees and 8 rays hit concrete structures, the spectral emissivity for concrete is used for the term ε_B.

Modification of atmospheric profiles

One final modification in this on-going research was the added capability to control the atmospheric profile input to the MODTRAN model based on the time of day. Upper air weather observation data can be used to specify the atmospheric profile description in the MODTRAN model. This data is typically collected at noon and midnight (GMT) at local airports. The restriction imposed by this collection schedule is that the profile specified is only valid for these two times. At intermediate collection time, many surface level parameters change, for example, surface temperature at the time of collection will almost certainly be different from the temperature at noon or midnight (GMT). For this reason, a capability to change the lower portion of the upper air weather observation data profile based on the recorded meteorological history was implemented. The meteorological data which is input to the THERM model (usually recorded on 15-minute intervals) is used to specify the boundary layer temperature, atmospheric pressure and dew point temperature of the radiosonde data. This procedure is illustrated in Figure 8 where the data up to the inversion layer altitude is modified via a linear interpolation for the temperature profile. The same procedure is carried out for pressure and dew point temperature.

RESULTS

In order to illustrate the enhancements to the DIRSIG model described in this paper, several illustrations have been prepared. The first is an image depicting an air field with several buildings and foxbat fighter planes. Figure 9 was generated to represent an image acquired with a panchromatic imaging system sensitive in the region 0.4 to 0.7 μm. This image depicts the effect of background objects obstructing the targets view of the sky above. If you look in the contrast enhanced images to the right, you can see radiance gradations in the grass regions adjacent to the buildings. These subtle changes in the upwelling radiance

field are due to a reduction in the amount of sky radiance which is falling onto the target due to the hemisphere of sky above the target being partially blocked, resulting in a shape factor for these individual pixels less than unity. As you move away from the building the radiance field increases in magnitude, indicating that more of the sky radiance is striking the target.

To illustrate the capabilities of the DIRSIG model (with the incorporation of MODTRAN atmospheric propagation) to depict sky radiance, a sensor positioned at a grazing angle such that a portion of the sky can be seen is simulated. The ground in this scene is simulated concrete with diffuse reflectance characteristics in the 0.4 to 0.7 μm wavelength region. The image is simulated on the summer solstice at 7 PM to capture a "sunset". The bright area which appears to be the sun is scattered energy near the solar source and not the sun itself since the MODTRAN model does not contain the source at a point in space. The variation in sky radiance with zenith and azimuth angles is very clear in this image.

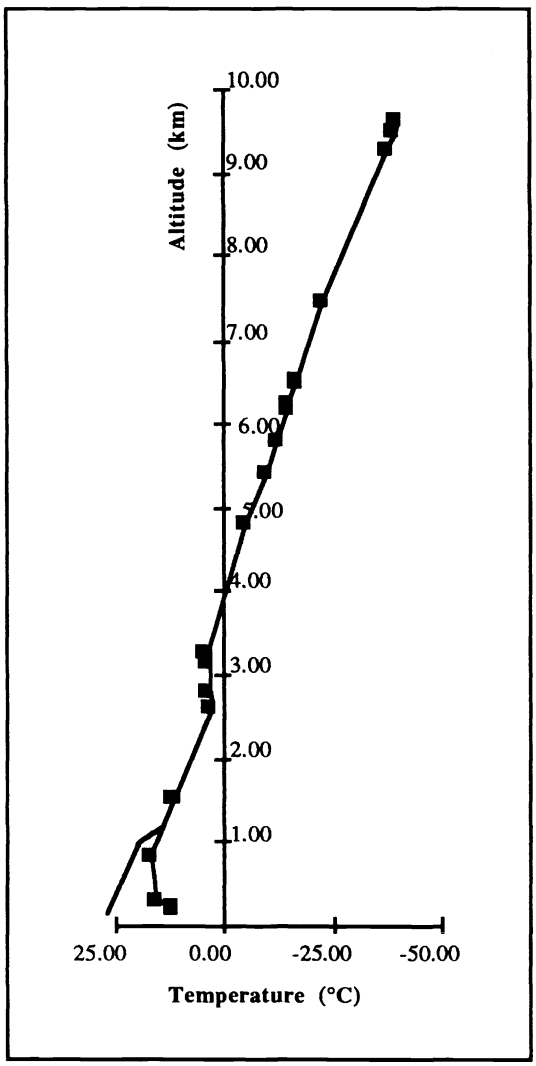

Figure 8 Illustration of the boundary layer modification to the user specified temperature profile input to the MODTRAN model.

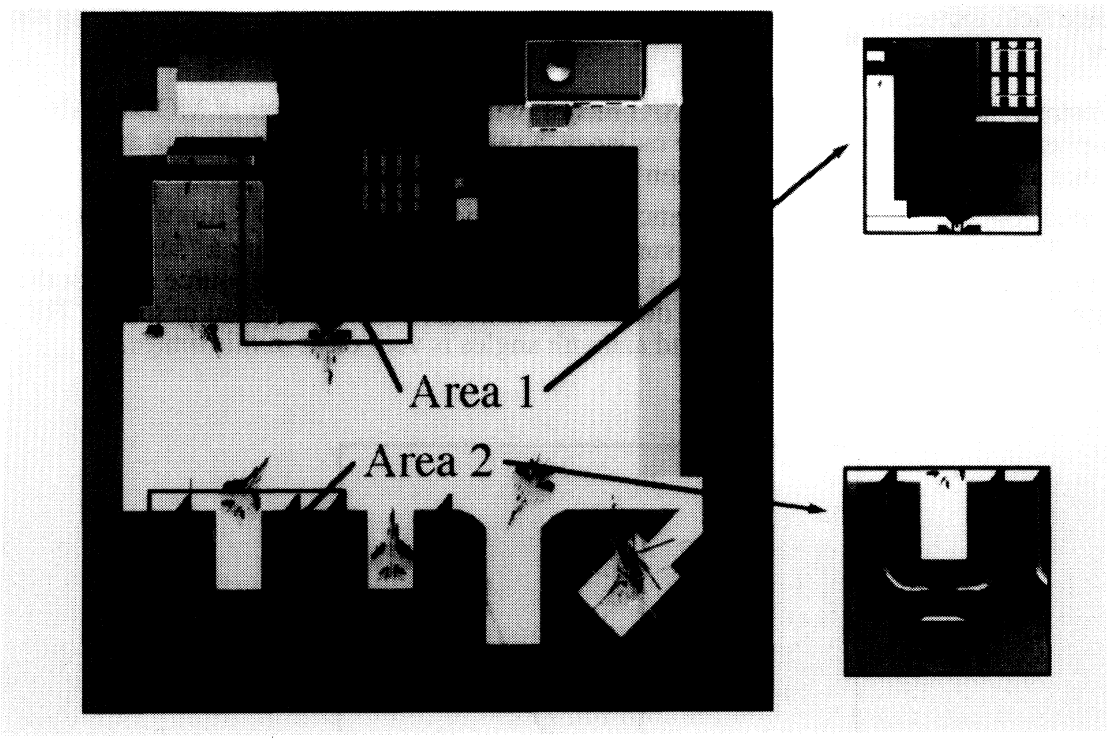

Figure 9 Panchromatic image (0.4 to 0.7 μm) enhanced to illustrate the radiometric effects which the shape factor computation have on the radiance field from diffuse objects with adjacent object interactions.

REFERENCES

AutoCAD Release 10 Reference Manual, Autodesk Inc., 1989.

Berk, A., L.S. Bernstein and D.C. Robertson, MODTRAN: A moderate resolution model for LOWTRAN 7, GL-TR-89-0122, Spectral Sciences, Inc., Burlington, Massechusetts, April 1989.

DCS Corporation, AIRSIM thermal signature prediction and analysis tool model assumptions and analytical foundations, DCS Technical Note 9090-002-001, 1991.

Haines, E., Essential ray tracing algorithms, *Introduction to Ray Tracing Short Course Notes*, 14th Annual Conference on Computer Graphics and Interactive Techniques, SIGGRAPH, Anaheim, California, July 1987.

Kneizys, F.X., E.P. Shettle, L.W. Abreu, J.H. Chetwynd, G.P. Anderson, W.O. Gallery, J.E.A. Selby, and S.A. Clough, *Users Guide to LOWTRAN 7*, AFGL-TR-88-0177, Environmental Research Papers, No. 1010, Air Force Geophysics Laboratory, Optical/Infrared Technology Division, Hanscom AFB, Maryland, August 1988.

Rankin, D.K., C. Salvaggio, T. Gallagher and J.R. Schott, Instrumentation and procedures for validation of synthetic infraed image generation models, Proceedings of the SPIE, Infrared Technology XVIII, Vol. 1762, July 1992, pp. 584-600.

Schott, J.R., R. Raqueno and C. Salvaggio, Incorporation of a time-dependent thermodynamic model and a radiation propagation model into infrared three-dimensional synthetic image generation, *Optical Engineering*, Vol. 31, No. 7, July 1992, pp. 1505-1516.

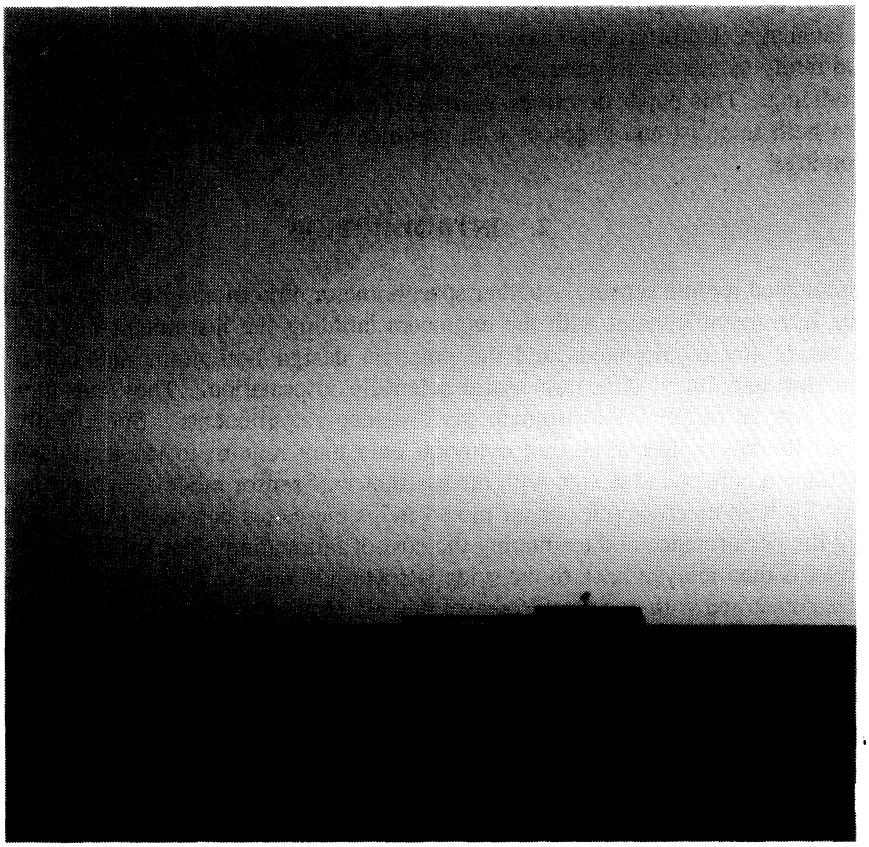

Figure 10 Panchromatic image (0.4 to 0.7 μm) from a west-facing sensor illustrating the prediction of sky radiance. The image simulates a collection on day 172 and 7 PM.